JOURNAL OF THE KOREAN ASTRONOMICAL SOCIETY
31: 161 ~ 171, 1998

A STUDY OF LYNDS 1299 DARK CLOUD

RYU, OK-KYUNG[1] AND LEE, YOUNGUNG[2]
[1]Department of Astronomy and Space Science, Chungnam National University, Taejon, Korea
okryu@astro6.chungnam.ac.kr
[2]Korea Astronomy Observatory, Taeduk Radio Astronomy Observatory, Taejon, Korea
yulee@hanul.issa.re.kr
(Received Oct. 2, 1998; Accepted Oct. 17, 1998)

ABSTRACT

We have mapped about 1.5 square degree regions of Lynds 1299, a well isolated dark cloud in the Outer Galaxy ($l = 122°, b = -7°$), in the $J = 1 - 0$ transition of ^{12}CO and ^{13}CO with the 13.7 m radio telescope at Taeduk Radio Astronomy Observatory (TRAO). We found that there are two velocity components in the molecular emission, at $V_{LSR} = -52$ km s^{-1} (Cloud A) and -8.8 km s^{-1} (Cloud B), respectively. We have derived physical parameters of two molecular clouds and discussed three different mass estimate techniques. We found that there are large discrepancies between the virial and LTE mass estimates for both clouds. The large virial mass estimate reflects the fact that both are not gravitationally bound. We adopt the mass of 5.6×10^3 $M_\odot$ for Cloud A and 1.2×10^3 $M_\odot$ for Cloud B using conversion factor. Cloud A is found to be associated with a localized star forming site, and its morphology is well matching with that of far-infrared (FIR) dust emission. It shows a clear ring structure with an obvious velocity gradient. We suggest that it may be a remnant cloud from a past episode of massive star formation. Cloud B is found to be unrelated to Cloud A (d = 800 pc) and has no specific velocity structure. The average dust color temperature of the uncontaminated portion of Cloud A is estimated to be 24~27.4 K. The low dust temperature may imply that there is no additional internal heating source within the cloud. The heating of the cloud is probably dominated by the interstellar radiation field except the region directly associated with the new-born B5 star. Overall, the dust properties of Cloud A are similar to those of normal dark cloud even though it does have star forming activity.

Key Words : Interstellar Medium; Dark Cloud; Velocity Structure; Far-Infrared Emission

I. INTRODUCTION

Lynds 1299 is a dark cloud located at $(l, b) = (122°, -7°)$ in the Outer Galaxy. The location of the Lynds 1299 is far above the Galactic plane ($b = -7°$), thus it is implicit that there may be little contamination with gas in Galactic plane. On both of the red and blue plates of Palomar Observatory Sky Survey (POSS) there is clear sign of nebulocity, which implies that star forming activity may be going on. In fact, there is a B5 star embedded at the location of IRAS point source 00420+5530, $(\alpha, \delta)_{1950} = (00^h42^m5^s.0, +55°31')$ (Neckel and Staude 1984). The far-infrared (FIR) emission map centered on Lynds 1299 shows a very intriguing feature. The strongest FIR emission arises at the exact position of the nebulocity, and it has a ring-like structure with a diameter of approximately 1° with some dispersed filamentary structure (see Figure 1). Continuum data of this object has not been reported. Existing HI data (Weaver & Williams 1973) is not suitable to compare with CO data as its beam size of 36′ is too large. Recently, Yonekura et al. (1997) mapped the large area including the Lynds 1299 in ^{13}CO $J = 1 - 0$ with a sampling rate of 8′. However, they detected only small portion of emission from the cloud as their sampling rate was too coarse. There is no other specific object associated with Lynds 1299. With all these privileges this cloud has never been studied in any molecular lines except Yonekura et al.'s study (1997).

In this paper, we have obtained a high resolution maps of Lynds 1299 in ^{12}CO and ^{13}CO. We use these data to study the velocity structure, mass, and kinematics of the cloud, and discuss the evolutionary status of the cloud which has a peculiar morphology. In section 2, observation mode is presented, and we discuss the observation results in section 3. In section 4 we discuss the results, and we summarize it in section 5.

II. OBSERVATIONS

We have mapped Lynds 1299 in the $J = 1 - 0$ transition of ^{12}CO and ^{13}CO with the 13.7 m radio telescope (FWHM=50″) at Taeduk Radio Astronomy Observatory (TRAO) on 1995 April, May, and December for ^{12}CO $J = 1 - 0$ and 1997 April and December for ^{13}CO $J = 1 - 0$. Sampling rate was 2′ and about 120′ × 90′ region was covered. About 1,900 spectra of ^{12}CO and 1,300 spectra of ^{13}CO were obtained. A SIS receiver equipped with an SSB filter was used for the frontend. The two filterbanks with 256 channels having a bandwidth of 250 KHz per channel were used. The corresponding velocity resolutions at the rest frequency of ^{12}CO and ^{13}CO are 0.65 km s^{-1} and 0.68 km s^{-1}, respectively.

All observations were made by repeatedly switching

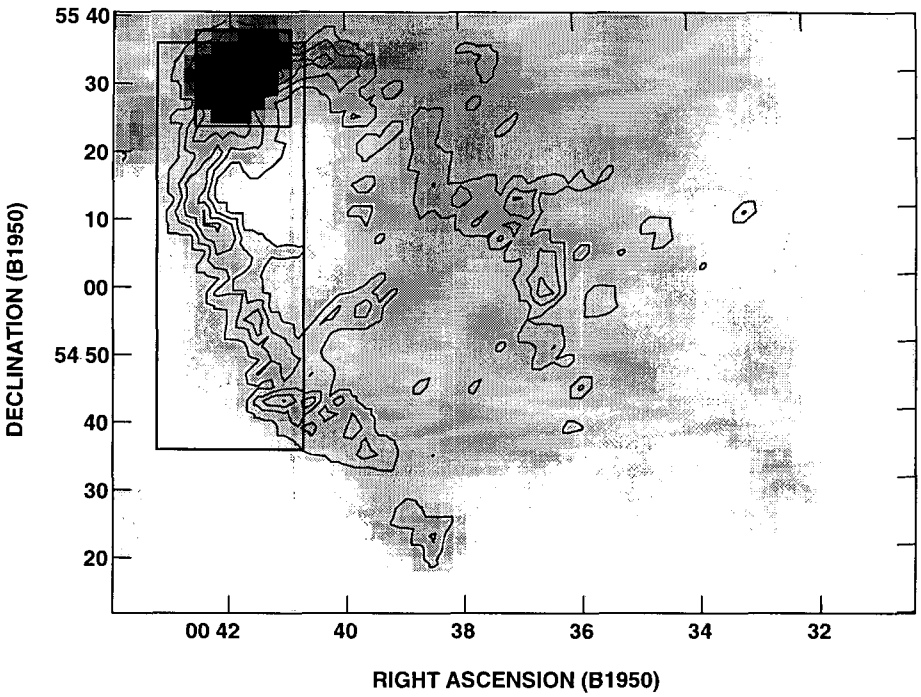

Fig. 1.— The ^{12}CO integrated intensity contour map of Cloud A superposed on the IRAS flux gray-scaled map at 100 μm. The gray-scale range is 15~45 MJy sr^{-1}. The lowest contour level is 1.4 K km s^{-1} and the increment between the levels is 4 K km s^{-1}. The larger solid box indicates the region to compare CO emission with FIR emission, and smaller one indicates the region of spectra shown in Figure 4.

to one reference position at $l = 121°$ and $b = -6°.5$ confirmed to have no CO emission. Calibration was accomplished by frequently observing an ambient temperature load. All antenna temperatures quoted are corrected for atmospheric extinction and for the forward spillover and scattering losses of the antenna and radome (η_{fss}= 0.68 at 110 to 115 GHz), and are therefore on the T_R^* temperature scale defined by Kutner and Ulich (1981). The average rms noise of the data in T_R^* unit was 0.2 K for ^{12}CO, and 0.1 K for ^{13}CO, respectively.

III. RESULTS

(a) Cloud Morphology and Velocity Structure

We found that there are two velocity components in the molecular emission at $V_{LSR} = -52$ km s^{-1} and -8.8 km s^{-1}. Two molecular clouds seems to be physically unrelated each other as there is a large velocity discrepancy of over 40 km s^{-1}. We nominate the component at $V_{LSR} = -52$ km s^{-1} as Cloud A, and for the component at $V_{LSR} = -8.8$ km s^{-1} as Cloud B.

i) Cloud A

The ^{12}CO integrated intensity contour map of Cloud A is presented in Figure 1, overlayed on the gray-scale map of FIR flux at 100 μm. The morphology of Cloud A is characterized by elliptical ring-like shape, which is well matching with FIR emission boundary, especially on the eastern part of the cloud. It has an extent of about 0°.8 × 1°.2 in Right Ascension and Declination direction. Assuming a distance of 1.7 kpc (Neckel and Staude 1984), the full size of the cloud is about 30 pc. The ^{12}CO peak temperature of the cloud is 10.7 K, and the ^{13}CO peak temperature is 4.1 K, which arises at the position of IRAS point source 00420+5530, where the star forming activity is going on. The ^{13}CO peak temperature map is presented in Figure 2. The ^{13}CO emission, which traces denser portion of the cloud, is mainly detected in the eastern part of the cloud mapped.

Figure 3 is the ^{12}CO channel map at individual velocities. The velocity coverage of each map is 0.65 km s^{-1}, which is corresponding to one channel of 250 KHz filterbank. The covered velocity range is $-55.7 \sim -47.2$ km s^{-1}. Figure 4 shows ^{12}CO and ^{13}CO spectra corresponding to region of the strongest ^{12}CO emission which is shown as a smaller solid box in Figure 1. The some of line profiles have non-gaussian shapes, which implies that there is significantly strong turbulence, especially at the star forming region. The linewidths are about 2 or 3 km s^{-1} in the calm region with gaussian line profiles, which is typically found in normal dark cloud. On the other hand, in the star forming region they are more than twice larger than that of calm region. In addition, Cloud A shows a clear velocity gra-

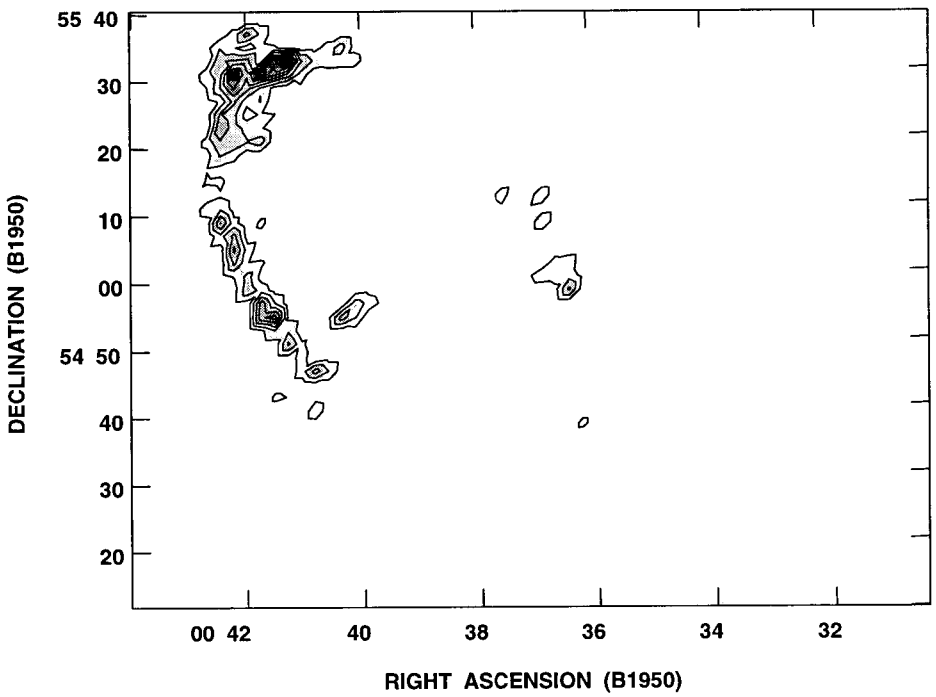

Fig. 2.— The ^{13}CO peak temperature map of Cloud A. The gray-scale range is 0.5~4 K, and the lowest contour level and the increment between levels are 0.5 K.

dient in ^{12}CO mean velocity map. The southern part is more blueshifted than the northern part of the cloud. This trend can be more evidently seen for the eastern part of the cloud, which is denser than the western part. To clarify the velocity gradient, we averaged the CO emission along the Right Ascension, and presented in Figure 5. In this spatial-velocity map, it is obvious that there is a velocity difference of about 1 km s^{-1} between the northern part and southern part of the cloud.

ii) Cloud B

The ^{12}CO integrated intensity map of Cloud B is presented in Figure 6. Comparing with the FIR emission presented in Figure 1, there is matching trend between the CO emission of Cloud B and FIR emission, though some portion is readily blended with that of Cloud A. Because of this blendness, we will not discuss the correlationship between FIR emission and CO emission for Cloud B. This cloud has also been detected on the survey of Yonekura et al. (1997), and its properties were briefly mentioned in their table. It has an extent of about 1°.3 × 1°.3 in Right Ascension and Declination direction. Assuming a distance of 800 pc (Yonekura et al. 1997), the full extent of the cloud is about 18 pc. The ^{12}CO peak temperature of the cloud is 6.7 K, and the ^{13}CO peak temperature is 1.8 K. The ^{13}CO peak temperature map is presented in Figure 7. The detected ^{13}CO emission regions are much smaller than that of ^{12}CO emission. Presumably, the cloud is not to be excited enough to emit strong ^{13}CO transition lines. Figure 8 is the ^{12}CO channel map at individual velocities. The velocity coverage of each map is 0.65 km s^{-1}, which is corresponding to one channel of 250 KHz filterbank, as in the case of Cloud A. The covered velocity range is $-12.2 \sim -5.0$ km s^{-1} and the mean velocity is about -8.8 km s^{-1}. Figure 9 shows some example of ^{12}CO and ^{13}CO spectra for the region marked with solid box in Figure 6. The ^{12}CO line widths of Cloud B are about 2 to 3 km s^{-1}, which corresponds to typical linewidths of normal dark cloud. The ^{12}CO mean velocity map and ^{12}CO position-velocity map are not presented in present paper. There is no specific velocity gradient in Cloud B.

(b) Mass Estimate

i) LTE Mass Estimate

The LTE mass estimate has been widely used to estimate cloud masses. This method and assumption inherent in its use had discussed in many papers (Lee 1992; Lee et al. 1994; Dickman 1978). The ^{13}CO column density is necessary to obtain the LTE mass. It can be determined when both ^{12}CO and ^{13}CO lines have been observed toward each line of sight.

For pixels with ^{13}CO emission greater than the 3 σ noise level, the column density of ^{13}CO in the i-th pixel

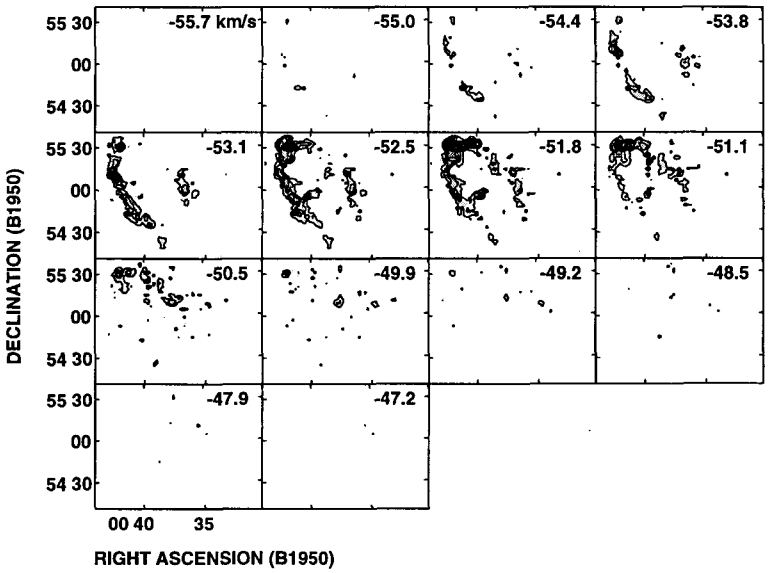

Fig. 3.— The ^{12}CO velocity map of Cloud A. Each map has V_{LSR} range of 0.65 km s^{-1}. The centered velocity of each map is marked at the upper-right corner. The lowest contour level is 1 K and the increment is 1.5 K. The gray scale ranges from 0 to 10.7 K.

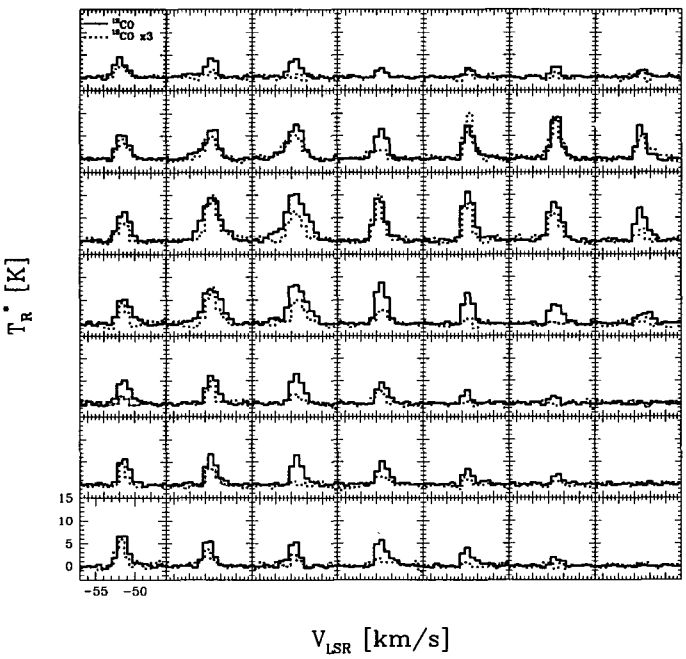

Fig. 4.— The ^{12}CO and ^{13}CO spectra corresponding to region of the strongest ^{12}CO emission which is shown as a smaller solid box in Figure 1.

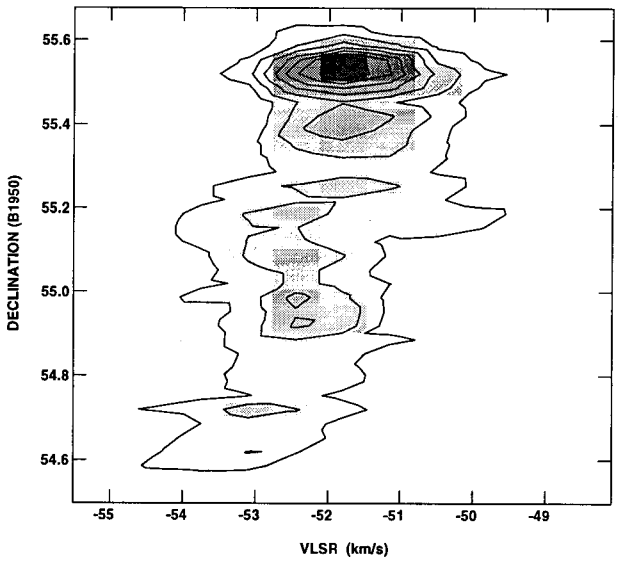

Fig. 5.— The ^{12}CO Declination-velocity maps averaged along the Right Ascension. The lowest contour level and the increment between levels are 0.2 K. The gray scale ranges from 0.2 to 1.8 K.

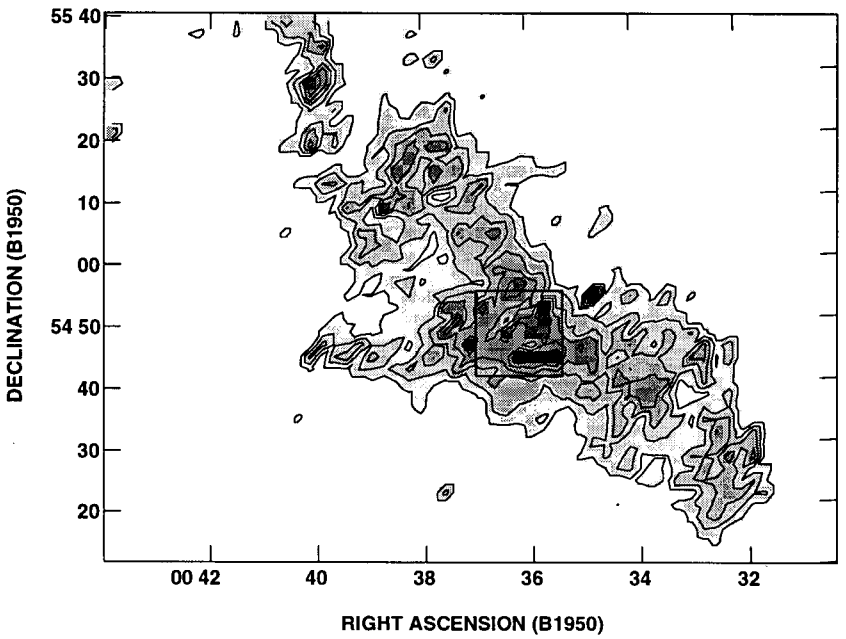

Fig. 6.— The ^{12}CO integrated intensity contour map of Cloud B. The gray-scale range is 0$\sim$12.5 K km s^{-1}. The lowest contour level is 1.2 K km s^{-1} and the increment between the levels is 1.68 K km s^{-1}. The solid box indicates the region of spectra shown in Figure 9.

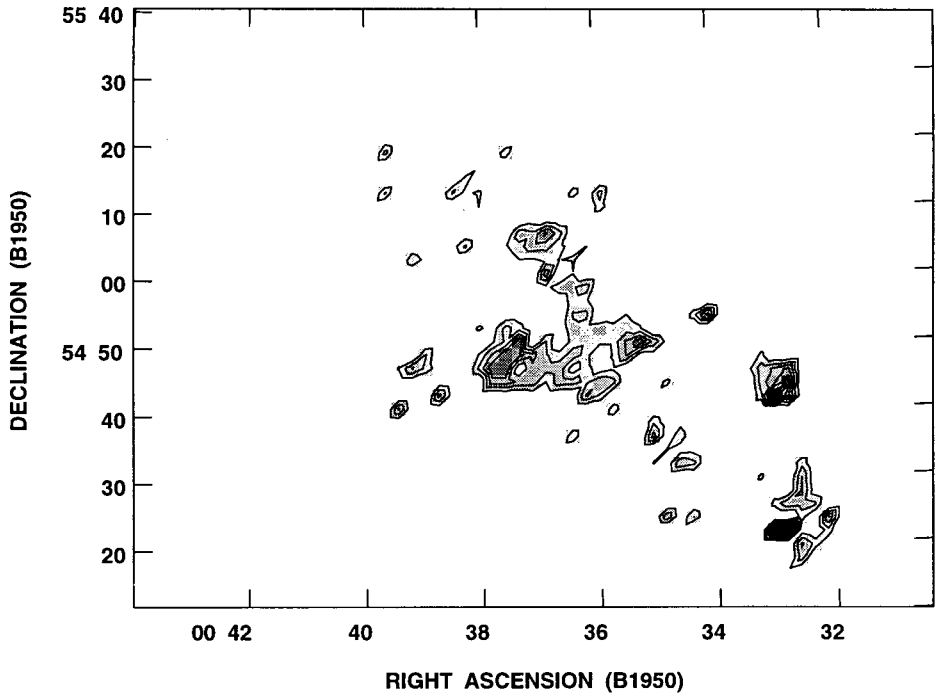

Fig. 7.— The ^{13}CO peak temperature map of Cloud B. The gray-scale range is 0.4~1.7 K, and the lowest contour level is 0.5 K, and the increment between level is 0.2 K.

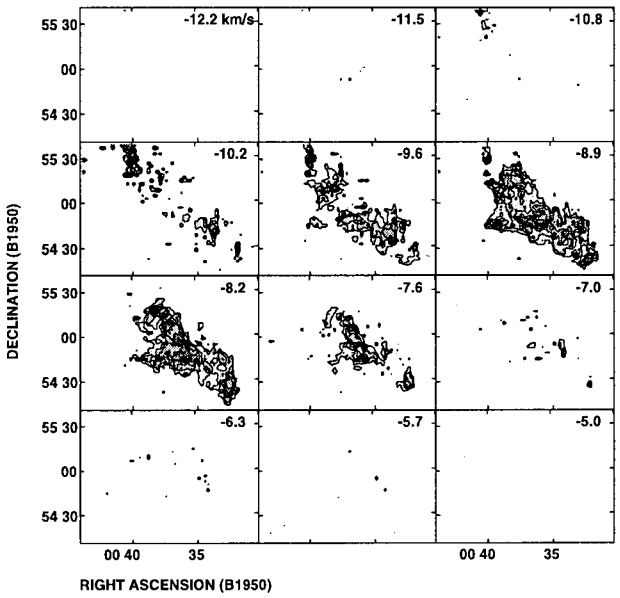

Fig. 8.— The ^{12}CO velocity map of Cloud B. Each map has V_{LSR} range of 0.65 km s^{-1}. The centered velocity of each map is marked at the upper-right corner. The lowest contour level and the increment are 1 K, respectively. The gray scale ranges from 0 to 6.7 K.

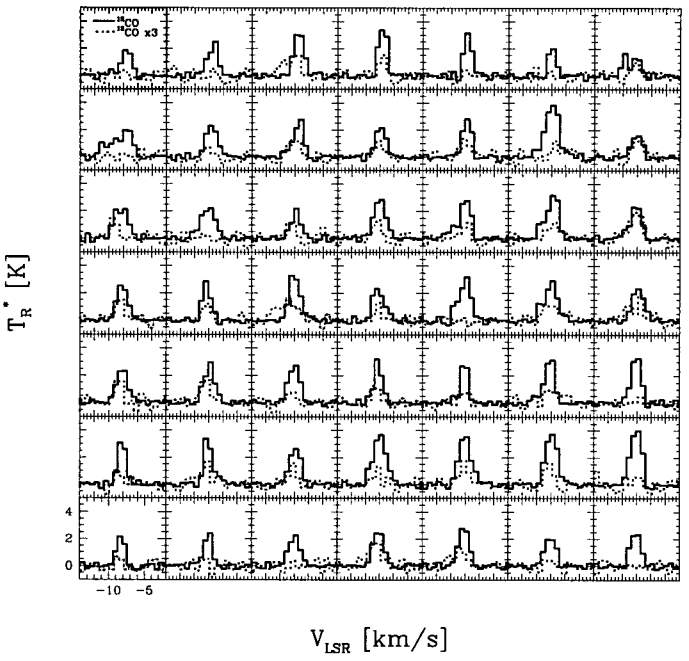

Fig. 9.— The ^{12}CO and ^{13}CO spectra for solid box in Figure 6.

of a cloud is given by

$$N(^{13}CO)_i = \frac{2.42 \times 10^{14} \Delta V_i \, T_{ex} \, \tau^{13}}{1 - \exp[-5.29/T_{ex}]} \quad [cm^{-2}], \quad (1)$$

$$\tau^{13} = -\ln\left[1 - \frac{T_R^{13}}{\frac{5.29}{e^{5.29/T_{ex}}-1} - 0.93}\right], \quad (2)$$

$$T_{ex} = \frac{5.53}{\ln\left[1 + \frac{5.53}{T_R^{12}+0.876}\right]}, \quad (3)$$

where ΔV_i is the full width at half-intensity in km s^{-1}, τ^{13} is the line center optical depth of ^{13}CO, and T_{ex} is the excitation temperature.

For pixels with emission weaker than the 3 σ noise level, the ^{13}CO column density is given by

$$N(^{13}CO)_i = \frac{3.76 \times 10^{14}}{f_u} \int T_R^*(^{13}CO) \, dv \quad [cm^{-2}], \quad (4)$$

where f_u is the fraction of ^{13}CO in the upper state ($J = 1$).

The obtained LTE mass is 1.5×10^3 M$_\odot$ for Cloud A, and 1.4×10^2 M$_\odot$ for Cloud B.

ii) Virial Mass Estimate

The partition of energy can be determined by the virial theorem, if a molecular cloud is virialized. The virial mass is given as

$$M_{VIR} = \frac{3 \, \beta \, \sigma_{tot}^2}{2 \, G} \, D, \quad (5)$$

$$\sigma_{tot} = \sqrt{\sigma_i^2 + \sigma_c^2} \quad [km \ s^{-1}], \quad (6)$$

$$D = \sqrt{(4A/\pi)} \quad [pc], \quad (7)$$

where σ_{tot} is velocity dispersion of the cloud, which represents all forms of kinetic motion within the cloud, σ_i is the internal velocity dispersion, and σ_c is the centroid velocity dispersion. The constant β is order of unity and depends on the shape and density distribution of the cloud. D is the cloud diameter and A is the area. It is not straightforward to define a cloud size as clouds have the irregular shape. The mean cloud diameter was adopted assuming a spherical cloud. The area of the cloud is defined as region covered by all pixels with ^{12}CO peak temperature greater than 5 σ.

In the case of Cloud A, the cloud size is 18.3 pc assuming that the cloud distance is 1.7 kpc (Neckel and Staude 1984) , and the internal and centroid velocity dispersions are 0.8 km s^{-1} and 0.9 km s^{-1}, respectively. Thus the total velocity dispersion is 1.2 km s^{-1}. For Cloud B, the cloud size is 11.6 pc assuming that the cloud distance is 800 pc (Yonekura et al. 1997), and the internal and centroid velocity dispersions 0.65 km s^{-1} and 0.56 km s^{-1}, respectively. Thus the total velocity dispersion is 0.86 km s^{-1}. The estimated virial mass is 1.5×10^4 M$_\odot$ for Cloud A, and 5×10^3 M$_\odot$ for Cloud B, assuming a uniform density distribution and a spherical cloud ($\beta \sim 1.6$).

iii) Mass from CO Luminosity

The mass using CO luminosity is based on the empirical relation between the CO integrated intensity

and molecular hydrogen column density, or the relation between CO luminosity and mass. This relationship has been studied by a number of investigators and reviewed by Scoville and Sanders (1987). In the CO luminosity–mass relation, empirical estimates of the conversion constant based on molecular observations vary between 1 and 5×10^{20} cm^{-2} (K km s^{-1})$^{-1}$ (Scoville and Sanders 1987). Usually the virial mass is used to calculate the conversion factor. In fact, a relation between total CO luminosity and cloud mass can be established theoretically if clouds are virialized (Dickman, Snell, and Schloerb 1986). The conversion factor has also been established through γ-ray studies (Lebrun et al. 1983; Bloemen et al. 1984; and summary by Bloemen 1989), which found similar conversion constant ranging from 2 to 3×10^{20} cm^{-2} (K km s^{-1})$^{-he}$. The γ-ray analysis suggests that the conversion factor is roughly constant throughout the Galaxy (Bloemen 1987). One merit of this method is that it is independent of virial mass estimates.

The ^{12}CO luminosity is calculated from the following equation

$$L = \Delta V_i \; T^i_{pk} \; A \quad [\mathrm{K\ km\ s^{-1}\ pc^2}], \tag{8}$$

where the sum is over all pixels, i, within the cloud boundary, $\Delta V_i (= (8\ln 2)^{1/2}\, \sigma_i)$ is the full width at half-intensity in velocity units, and A is the pixel area in units of pc^2.

The ^{12}CO luminosity is about 1,200 K km s^{-1} for Cloud A, and 250 K km s^{-1} for Cloud B. Thus the mass obtained from CO luminosity is 5.6×10^3 M$_\odot$ for Cloud A, and 1.2×10^3 M$_\odot$ for Cloud B. Here we use the most recent estimate of the conversion factor, 2.3×10^{20} cm^{-2} (K km s^{-1})$^{-1}$, established through γ-ray analysis (Bloeman 1989).

(c) Density

We used two methods to determine the cloud density. One is the volume density computed with the mass estimates, and the other is the density based on column density and line-of-sight distance. The average volume density is useful in the global cloud. We assumed that the clouds have spherical shape to estimate the average density roughly. The mass and size for Cloud A are 5.6×10^3 M$_\odot$ and 18.3 pc, respectively. The volume density of Cloud A is about 40 cm^{-3}. For Cloud B, the mass and size are 1.2×10^3 M$_\odot$ and 11.6 pc, and the volume density is about 33 cm^{-3}. The average volume density of dark clouds in solar neighborhood ranges from hundred to few thousand per cubic centimeter. Thus, the volume densities estimated for both clouds are much smaller than that of the density range of dark clouds.

Another method of the density estimate was obtained as follows. The average density along the line of sight is given by the H_2 column density, which is obtained from ^{13}CO column density, divided by the line-of-sight distance. We temporarily assumed that the line-of-sight distance equals the cloud size mentioned in previous method (as the cloud is well extended, the assumption may be exaggerated). In the case of Cloud A, the H_2 column density is 2.1×10^{21} cm^{-2}, and the line-of-sight distance is 18.3 pc. Thus, the average density of Cloud A is 38 cm^{-3}. The H_2 column density and the line-of-sight distance for Cloud B are 9×10^{20} cm^{-2} and 11.6 pc, respectively. Thus the average density of Cloud B is about 26 cm^{-3}.

(d) Far-Infrared Analysis

i) Relation to CO Emission

The CO emission and dust have spatial coincidence and morphological similarity for isolated clouds (Heyer et al. 1987; Langer et al. 1989; and Mooney 1992). It is necessary to separate the Galactic background FIR contamination from the cloud emission to estimate the FIR emission of the cloud accurately. However, the identification of the FIR emission is straightforward in the case of Lynds 1299 as the cloud is well isolated. The problem is that there are two different cloud components overlapped. Thus we extract the small portion of the region the CO emission of which is well matching with the FIR emission. It is marked with larger solid box of Figure 1. We compared CO emission with FIR emission at 100 μm and 60 μm for the region extracted. We present their correlationship in Figure 10. The scattered points above the main congregation are from the strong IRAS point sources, and thus not included in the least-squares fit. It is found that there is a good correlation between the FIR emission and the ^{12}CO integrated intensity for this region, except contribution of the IRAS point source, below 40 MJy sr^{-1} for 100 μm and below 15 MJy sr^{-1} for 60 μm. A least-squares fit was used to determine the relation between ^{12}CO integrated intensity and FIR flux.

The results of least-squares fits are shown as the solid line in Figure 10. The equations of the fitted lines are given as

$$I_{100} = 0.33(\pm 0.03)\; I_{CO} + 22.9(\pm 0.18), \tag{9}$$

$$I_{60} = 0.12(\pm 0.02)\; I_{CO} + 3.81(\pm 0.17), \tag{10}$$

where the FIR intensity has units of MJy sr^{-1} and the CO intensity has units of K km s^{-1}. The intercepts in the correlationship represent general foreground or background FIR emission from dust within the Galactic plane to this region. The slope represents the true relation between ^{12}CO integrated intensity and FIR intensity.

ii) Dust Temperature

A dust color temperature can be derived from the integrated flux density ratio at 60 and 100 μm, assuming that a dust emissivity law is proportional to $\lambda^{-\beta}$. The derived equation is given as

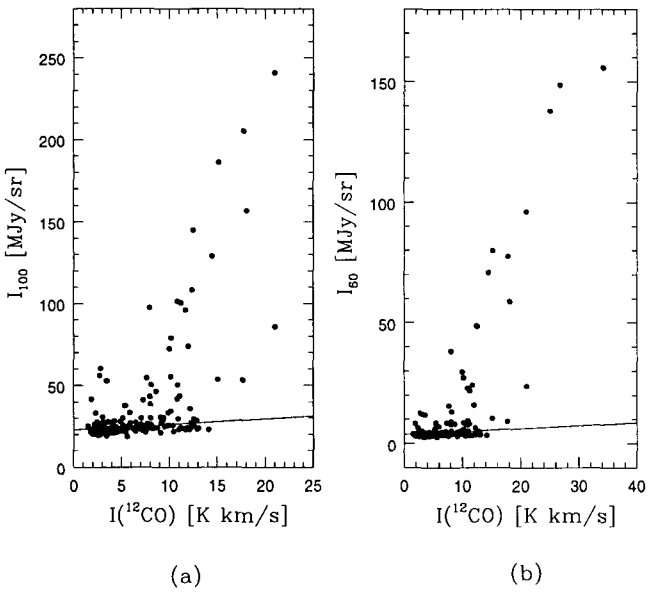

Fig. 10.— (a) The 100 μm intensity and (b) 60 μm intensity as a function of $I_{^{12}CO}$ for a larger solid box region in Figure 1. The solid lines are the results of the least squares fits.

$$\frac{S_{60}}{S_{100}} = \left(\frac{\lambda_{60}}{\lambda_{100}}\right)^{3+\beta} \left[\frac{\exp(hc/\lambda_{100}kT_d) - 1}{\exp(hc/\lambda_{60}kT_d) - 1}\right], \quad (11)$$

$$T_d = \frac{(hc/k)[1/\lambda_{60} - 1/\lambda_{100}]}{\ln[(S_{100}/S_{60})(\lambda_{100}/\lambda_{60})^{3+\beta}]}, \quad (12)$$

where β is emissivity index. The emissivity index is not well determined at these wavelengths, but it probably ranges between β=1 (Hildebrand 1983) and β=1.5~2 (Cox & Mezger 1989). We obtained the flux density for the region not to be superposed between two clouds. The average flux density ratio of 60 to 100 μm for this region is 0.23. Thus the dust color temperature obtained from this ratio is 27.4 K assuming that the dust emissivity index is 1, and 24 K assuming that β=2. For star-forming clouds, the average flux density ratio is 0.53 (Carpenter, Snell, & Schloerb 1990). For nearby dark clouds, for example, the flux density ratios found for the two Taurus clouds of B18 and Heiles's cloud 2 are 0.17 and 0.12, respectively (Snell et al. 1989). Thus, the dust color temperature for the given region is more similar to that found in the cold dark clouds.

IV. DISCUSSION

(a) Mass and Density

The cloud mass was estimated in three different ways. For Cloud A, the LTE mass, 1.5×10^3 $M_\odot$ is the smallest and the virial mass, 1.5×10^4 $M_\odot$, is the largest. The difference between the two mass is a factor of 10. For Cloud B, the difference is much larger; the LTE mass, 1.4×10^2 $M_\odot$, is the smallest and the virial mass, 5×10^3 $M_\odot$, is the largest. Many parameters such as velocity dispersion, size, and density enter the virial mass estimate, and thus many sources of uncertainty are involved in this estimate. These parameters have been discussed in other paper (Lee 1992, 1994a). According to Lee (1994a, 1994b), these parameters will not affect virial estimate significantly if a cloud is virialized, though the velocity dispersion is the most important parameter. A factor of two or even three difference between mass estimates could easily be attributed to the uncertainties in these mass estimates. If this is the case, the cloud is likely to be virialized. However, the difference between mass estimates for two clouds in present study is too large. This fact reflects that both are not likely to be virialized.

Usually, the LTE mass estimate is the smallest. LTE mass estimate may significantly misses the mass outside the cloud boundary, and it is based on several critical assumptions. Thus, the LTE mass is usually underestimated. This mass estimate has also been discussed in many other papers (Lee, Snell, and Dickman 1990; Lee 1994a). A general relation between mass and CO luminosity may exist if the cloud is in virial equilibrium. However, if not in virial equilibrium, this method could overestimate the cloud mass. In the CO luminosity–mass relation we have used a recent estimate of the conversion factor, which was determined without considering virialization assumption; It is 2.3×10^{20} cm^{-2} (K km s^{-1})$^{-1}$, obtained from the γ-ray analysis (Bloeman 1989).

Both clouds are presumably not to be excited enough to detect the ^{13}CO emission. The LTE mass of two clouds in present study is quite underestimated. Especially, the detected ^{13}CO region for Cloud B is very small. Also, as the two clouds are not virialized, the virial mass estimates are not eligible as mass estimate. Thus, we adopt the masses of two molecular clouds using conversion factor from γ-ray analysis; 5.6×10^3 $M_\odot$ for Cloud A, and 1.2×10^3 $M_\odot$ for Cloud B.

The estimated densities must be a lower limit; the most important parameter to estimate the cloud density is the size of the cloud through the line of sight in this study. In fact, our assumption of the size along the line of sight must be an upper limit, as the cloud itself is expanding, and the cloud morphology is very dispersed. Thus, the actual dimension of the cloud should be smaller along the line of sight. The more accurate estimate of density can be done by studying CS emission and core structure, which we did not conduct in

this study.

(b) Velocity Field and Evolutionary Status of Cloud A

Cloud B may be the local cloud which shows no specific velocity field. Thus we will not discuss on Cloud B furthermore. On the other hand, Cloud A shows a elliptical ring structure, a very exceptional feature, seldom found in other molecular clouds. In addition, this ring structure shows a systematic velocity gradient; the velocity difference between northern part and southern part of the cloud is about 1 km s^{-1}. The possible mechanism for this peculiar velocity field may be explained only as expansion feature. If this is a projected velocity difference, it is expanding with a velocity of at least 1 km s^{-1}. However, there is no clear energy source inducing expansion within or around the cloud. What can be the energy source inducing expansion in the cloud? If the expanding velocity and size of the cloud are 1 km s^{-1} and about 30 pc, the expanding period and kinematic energy are 3.0×10^7 yr and 2.9×10^{46} ergs, respectively. The early type star can produce the huge kinematic energy of up to 10^{47} ergs. Thus, the beginning of the cloud expansion could be initiated by past formation of massive star or a combination of massive stars, and this energy may be sufficient to drive the surrounding molecular cloud to expand. Thus, we suggest that the evolutionary status of the ring structure may be explained as in the case of giant molecular clouds, G216-2.5 and Gem OB1 (Lee et al. 1994). According to them, G216-2.5 possesses broad line widths, very low gas temperatures, and no massive star formation, which are similar to the features of Lynds 1299 in small scale. Moreover, G216-2.5 has a very complicated and striking velocity structure. This giant molecular cloud may undergo episodic massive star formation events. Mooney (1992) also described a supporting scenario as follows; Giant molecular clouds undergo a massive star formation burst, fragment and expand, and then appear as quiescent cold clouds with the fossil remains of the past burst of star formation. Lee et al. (1994) suggested that G216-2.5 is a remnant cloud from a past episode of massive star formation.

We apply above explanation for the evolutionary status of G216-2.5 to the cloud in present study, though its scale is much smaller. We describe a scenario as follows: The cloud undergo a massive star formation with strong stellar wind, and the maternal molecular cloud was disrupted with part of cloud expanded. Then, the star within the cloud was evolved and dissipated, and the ring-like morphology is being remained as a remnant of original cloud. This is a fossil remains of episodic scenario of star formation. The new-born B5 star residing at the edge of the cloud may be a star of second generation. Thus, the evolutionary status of the cloud with ring-like structure may be inferred as the fossil remains of the past strong stellar wind or burst of massive early type star(s).

(c) Relation between FIR Emission and CO Emission

The comparison between CO emission and FIR emission is made for the region extracted as explained in section 3. A good correlation between the FIR intensity and the ^{12}CO integrated intensity exists in this region as in the case of dark clouds. The linear relations between 100 μm intensity and either the HI column density in regions of atomic gas or CO column density in molecular clouds have been found (Boulanger & Perault 1988; Snell, Heyer, & Schloerb 1989). Boulanger & Perault (1988) reported the results of a comparison between CO and FIR emission in nearby molecular clouds. They reported that the ratio between 100 μm intensity and CO integrated intensity in outside star forming regions range 0.7~2.5 (MJy sr^{-1}) (K km s^{-1})$^{-1}$. The average ratio obtained for the region of present study is 0.33 (MJy sr^{-1}) (K km s^{-1})$^{-1}$, which is substantially less than the value found by Boulanger & Perault (1988). We computed the ratio of 100 μm intensity to total hydrogen column density from the slope of the least-squares fit. The CO conversion factor established throughout the γ-ray analysis (Bloemen 1989) of 2.3×10^{20} H_2 cm^{-2} (K km s^{-1})$^{-1}$ is used to convert the CO intensities to molecular hydrogen column densities. The ratio of 100 and 60 μm intensity to the hydrogen column density computed for the region of present study are 0.08 and 0.027 MJy sr^{-1} (10^{20} H cm^{-2})$^{-1}$. These values can be compared to those for normal dark clouds. For example, $I_{100\mu m}/N(H)$ and $I_{60\mu m}/N(H)$ are 0.07 and 0.012 for B18, and 0.10 and 0.012 MJy sr^{-1} (10^{20} H cm^{-2})$^{-1}$ for HCL2, respectively (Snell, Heyer, & Schloerb 1989). The ratios obtained for the region of present study are comparable to the dark cloud ratios. Snell et al. (1989) attributed the low ratios in the dark clouds to dust heated by only the solar neighborhood interstellar radiation field. Mooney (1992) also found a similar conclusion for the clouds classified as IR-quiet. Thus, the unusually low ratios obtained in present paper is probably due to the absence of internal heating sources. The B5 type star within the cloud may not have enough energy to heat the associated dust and gas in large scale. Thus, the dust temperature should also be relatively low.

V. SUMMARY

We have mapped L1299 in $J = 1 - 0$ transition of ^{12}CO and ^{13}CO with 13.7 m radio telescope at Taeduk Radio Astronomy Observatory (TRAO). We summarize our main results as follows;

1. We found that there are two velocity components in the molecular emission at $V_{LSR} = -52$ km s^{-1} (Cloud A) and -8.8 km s^{-1} (Cloud B). The two molecular clouds are physically unrelated each other as they have the velocity difference of over 40 km s^{-1}. Cloud B is presented the Local Cloud with no specific velocity structure. Cloud A shows a elliptical ring structure,

well matching with the FIR emission.

2. For both clouds there are large mass discrepancy in three mass estimates. The virial mass estimates are the largest, and the LTE mass estimates are the smallest. The large virial masses may reflect the fact that both molecular clouds are not gravitationally bound. Thus, we adopt the cloud mass using conversion factor determined from γ-ray analysis; 5.6×10^3 $M_\odot$ for Cloud A and 1.2×10^3 $M_\odot$ for Cloud B.

3. We obtained a good correlationship between the FIR emission and CO emission for the portion of Cloud A, which are thought to be uncontaminated from other sources. The flux density ratio of 100 μm to 60 μm is 0.23, and the dust color temperature is 24~27.4 K, which are similar to those found in the cold dark cloud. Both the low ratio and low dust temperature are likely due to the lack of internal heating sources. The star forming region within the cloud may be affected the whole region of the cloud only a little. The dust heating is probably dominated by the interstellar radiation field.

4. The velocity structure of the cloud with a ring-like shape can be explained with expansion. The expansion period and kinematic energy computed from the size and expansion velocity of the cloud present the fact that it is sufficient if the energy source induced expansion is the massive early type star(s). Thus, the evolutionary status of ring structure may be explained as in the case of giant molecular clouds, G216-2.5 and Gem OB1. We suggest that it may be a remnant cloud from a past episode of massive star formation.

REFERENCES

Bloemen, J. B. G. M., Caraveo, P. A., Hermsen, Lebrun, F., Maddalena, R. J., Strong, A. W., & Thaddeus, P. 1984, A&A, 139, 37

Bloemen, J. B. G. M. 1987, in Interstellar Process, ed. D. J. Hollenbach & H. A. Thronson, Jr.(Dordrecht: Reidel), 143

Bloemen, J. B. G. M. 1989, ARA&A, 27, 469

Boulanger, F., & Perault, M. 1988, ApJ, 330, 964

Carpenter, J. M., Snell, R. L., and Schloerb, F. P. 1990, ApJ, 224, 132

Cox, P. & Mezger, P. G. 1989, AAR, 1, 49

Dickman, R. L. 1978, ApJS, 37, 407

Dickman, R. L., Snell, R. L., & Schloerb, F. P. 1986, ApJ, 306, 326

Heyer, M. H., Vrba, F. J., Snell, R. L., Schloerb, F. P., Strom. S. E., Goldsmith, P. F., and Strom, K. M. 1987, ApJ, 321, 855

Hildebrand , R. H. 1983, Quart. J. Roy. Ast. Soc., 24, 267

Kutner, M. C., & Ulich, B. L. 1981, ApJ, 250, 341

Langer, W., Wilson, R. W., & Goldsmith, P. F. 1989, ApJ, 337, 355

Lebrun, F., Bennet, K., Bignami, G., Bloemen, J. B. G. M., & Buccheri, R. 1983, ApJ, 281, 634

Lee, Y., Snell, R. L., & Dickman, R. L. 1990, ApJ, 355, 536

Lee, Y. 1992, Ph. D. Dissertation, University of Massachusetts, Amherst

Lee, Y., Snell, R. L., & Dickman, R. L. 1994, ApJ, 432, 167

Lee, Y. 1994a, Publications of the Korean Astronomy Society, Vol. 9, No. 1, 55

Lee, Y. 1994b, Journal of the Korean Astronomy Society, Vol. 27, No. 2, 147

Mooney, T. 1992, Ph.D. thesis, Univ. New York, Stony Brook

Neckel, T., & Staude, H. J. 1984, A&A, 131, 200

Scoville, N. Z., & Sanders, D. B. 1987, in Interstellar Processes, ed. D. J. Hollenbach & H. A. Thronson, Jr.(Dordrecht: Reidel), 21

Snell, R. L., Heyer, M. H., & Schloerb, F. P. 1989, ApJ, 337, 739

Weaver, H. F. and Williams, D. R. W. 1973, A&AS, 8, 1

Yonekura, Y., Dobashi, K., Mizuno, A., Ogawa, H., & Fukui, Y. 1997, ApJS, 110, 21